



Title	Sensitivity kernels for finite-frequency surface waves
Author(s)	Yoshizawa, K.; Kennett, B. L. N.
Citation	Geophysical Journal International, 162(3), 910-926 <a href="https://doi.org/10.1111/j.1365-246X.2005.02707.x">https://doi.org/10.1111/j.1365-246X.2005.02707.x</a>
Issue Date	2005
Doc URL	<a href="http://hdl.handle.net/2115/52164">http://hdl.handle.net/2115/52164</a>
Type	article
File Information	j.1365-246X.2005.02707.x.pdf



[Instructions for use](#)

# Sensitivity kernels for finite-frequency surface waves

K. Yoshizawa<sup>1</sup> and B. L. N. Kennett<sup>2</sup>

<sup>1</sup>*Division of Earth and Planetary Sciences, Hokkaido University, Sapporo 060-0810, Japan. E-mail: kazu@ep.sci.hokudai.ac.jp*

<sup>2</sup>*Research School of Earth Sciences, Australian National University, Canberra, ACT 0200, Australia*

Accepted 2005 June 8. Received 2005 May 13; in original form 2004 March 19

## SUMMARY

Sensitivity kernels for fundamental mode surface waves at finite frequency for 2-D phase speed and 3-D shear wave speed are constructed based on the Born and Rytov approximations working with a potential representation for surface waves. The use of asymptotic Green's functions for scalar wave equations provides an efficient way to calculate the Born or Rytov kernels. The 2-D sensitivity kernels enable us to incorporate the finite-frequency effects of surface waves, as well as off-great-circle propagation, in tomographic inversions for phase-speed structures. We derive examples of the 2-D sensitivity kernels both for a homogeneous background model (or a spherically symmetric model), and for a laterally heterogeneous model. The resulting distortions of the shape of the sensitivity kernels for a heterogeneous background model indicate the importance of the use of proper kernels to account of the heterogeneity in the real Earth. By combining a set of 2-D sensitivity kernels with 1-D vertical sensitivity kernels for a particular frequency range and taking the inverse Fourier transform, we can derive 3-D sensitivity kernels for surface waves in the time domain. Such 3-D kernels are useful for efficient forward modelling of surface waveforms incorporating finite-frequency effects, and will also enable us to perform direct inversion of surface waveforms into 3-D structure taking account of finite-frequency effects.

**Key words:** diffraction, ray theory, scattering, sensitivity, surface waves, tomography.

## 1 INTRODUCTION

The theoretical basis of most surface-wave tomography has been geometrical ray theory. This simplified approach allows us to treat a large number of data to produce 3-D upper mantle models in an efficient manner. One of the well-known limitations of such ray theory is that the theory is no longer valid if the scale length of lateral heterogeneity is close to the wavelength to be used. To overcome this limitation, a number of methods that include the effects of scattering and diffraction in tomographic inversions have been proposed.

Studies on the diffraction and scattering of seismic waves have been tackled by many researchers based mainly on single scattering theory using the Born and Rytov approximations. Tomographic inversion considering the diffraction effects of seismic wave propagation was introduced by Devaney (1984) in the context of exploration geophysics based on his method of diffraction tomography for ultrasound waves. Wielandt (1987) discussed the effects of diffraction on body wave traveltimes, and showed that diffracted waves could have noticeable amplitudes and that the simple ray approximation breaks down in such circumstances.

For surface waves, Yomogida & Aki (1987) initiated tomographic inversion with finite-width kernels derived from an asymptotic formulation in terms of Gaussian beams for surface waves (Yomogida 1985; Yomogida & Aki 1985). They produced 2-D sensitivity kernels for phase-speed structure based on the Born and Rytov approximations and applied them to the reconstruction of phase-speed maps in the Pacific region using both the phase and amplitude of surface waves. Tanimoto (1990) tackled this problem with an alternative approach using potential theory, and indicated how to take account of inter-mode conversion of surface waves. This potential representation was further extended by Tromp & Dahlen (1993) to be able to accommodate local radial eigenfunctions.

Sensitivity kernels for body wave traveltimes or waveforms at finite frequency have been proposed by many researchers (Luo & Shuster 1991; Woodward 1992; Yomogida 1992; Vasco & Majer 1993; Li & Tanimoto 1993; Li & Romanowicz 1995; Marquering & Snieder 1995; Friderich 1999; Marquering *et al.* 1999; Dahlen *et al.* 2000; Zhao *et al.* 2000). Working with such kernels, several tomography models taking account of finite-frequency effects have been proposed (e.g. Li & Romanowicz 1996; Gung & Romanowicz 2004; Montelli *et al.* 2004). Meier *et al.* (1997) proposed a way to perform inversion for surface waves considering diffraction effects based on both the WKBJ approximation and the first Born scattering theory of Snieder (1986) and Snieder & Nolet (1987). Marquering *et al.* (1998) have also used linearized scattering theory to calculate 3-D waveform sensitivity kernels. Marquering *et al.* (1999) calculated body-wave traveltime kernels using waveform

kernels based upon surface-wave mode coupling. Dahlen *et al.* (2000) and Hung *et al.* (2000) reformulated the body wave traveltime kernels using Born scattering for body waves. Zhao *et al.* (2000) proposed body wave traveltime kernels based on normal mode theory and suggested that the sensitivity on the central ray path is smaller than the surrounding area, but not exactly zero as in the sensitivity kernels derived from the ray theory. There are also several studies tackling more complicated effects of multiple scattering (Friderich 1999; Maupin 2001).

Recently, Spetzler *et al.* (2002) derived sensitivity kernels based on Rytov approximation working with the surface-wave-scattering theory of Snieder & Nolet (1987). Zhou *et al.* (2004) proposed sensitivity kernels for surface-wave observables, that is, phase, amplitude and polarization anomaly data, taking account of the effects of coupling between mode branches.

Yoshizawa & Kennett (2002) have recently developed a technique of Fresnel-area ray tracing for surface waves based on the work of Červený & Soares (1992), and obtained paraxial Fresnel areas around the central ray path, introducing the concept of the *influence zone* in which wavefields are coherent in phase that does not depend on first-order scattering approximation. The influence zone has been applied to the reconstruction of a finite-frequency tomography model in the Australian region (Yoshizawa & Kennett 2004). The major target of the influence zone is somewhat different from the other studies on the surface wave scattering because the influence zone in our definition simply represents the sampling regions around the central ray path, for which surface waves propagating along different paths are coherent in phase. Since the influence zone represents a very narrow region (i.e. one-third of the width of the first Fresnel zone), the full effects of scattering and diffraction in the entire region around the path have not been considered.

In order to investigate how the velocity structure affects the surface wavefield, in this paper, we first derive simple expressions for the sensitivity kernels of surface waves based on the Born and Rytov approximations (e.g. Born & Wolf 1999) using a surface-wave-potential representation following Tanimoto (1990) and Tromp & Dahlen (1993). The general forms of these kernels are similar to those given by Yomogida & Aki (1987), Woodward (1992) and Snieder & Lomax (1996). We then employ asymptotic Green's functions for explicit formulations of the sensitivity kernels. The Born kernels are directly related to the perturbation of the potentials, whereas the Rytov kernels are related to the logarithm of the potentials, which yields a separation of the log amplitude term and the phase term of the surface wave potential. We show some examples of 2-D sensitivity kernels for surface-wave phase speed in media with both homogeneous and heterogeneous backgrounds.

Furthermore, we develop an efficient way to derive 3-D sensitivity kernels of the fundamental mode surface waves in the time domain, utilizing the 2-D sensitivity kernels for phase speed and the 1-D sensitivity for local shear wave-speed structure. Such time-dependent 3-D kernels represent regions of sensitivity in 3-D space that affect the surface wavefield in three dimensions. The 3-D kernels allow us to directly invert suitably bandpass filtered seismograms for a 3-D shear wave-speed structure.

Recent work by Zhou *et al.* (2004) proposed 3-D sensitivity kernels for surface-wave observables based on a single scattering theory, presenting several classes of the 3-D sensitivity of surface-wave information measured with a practical method such as a multitaper technique (e.g. Laske *et al.* 1994). In this study, our major objective is to investigate an alternative approach for constructing sensitivity kernels working with a potential representation for surface waves. We present general descriptions and features of sensitivity kernels for surface-wave phases in a 2-D phase-speed distribution, and for waveforms of surface waves in a 3-D shear wave-speed structure, which enables us to perform direct inversion of observed waveforms. Furthermore, we develop the sensitivity kernels not only for a homogeneous background structure, but also for a heterogeneous background structure.

## 2 GENERAL EXPRESSIONS FOR SENSITIVITY KERNELS BASED ON SINGLE SCATTERING THEORY

### 2.1 Born approach

Following Tanimoto (1990) and Tromp & Dahlen (1993), Love and Rayleigh wave displacement fields in laterally slowly varying media can be approximately represented in terms of surface-wave potentials  $\chi$ , which satisfy a spherical Helmholtz equation,

$$\mathbf{u}_R = \mathbf{r}U(r)\chi_R + k_R^{-1}V(r)\nabla_1\chi_R, \quad (1)$$

$$\mathbf{u}_L = k_L^{-1}W(r)(-\mathbf{r} \times \nabla_1)\chi_L, \quad (2)$$

where  $U$ ,  $V$ ,  $W$  are radial eigenfunctions as a function of radius  $r$ ,  $\mathbf{r}$  is a unit vector defined on a unit sphere,  $\nabla_1$  is a surface gradient operator, subscript  $R$  stands for Rayleigh waves, and  $L$  for Love waves. Hereafter, we omit these subscripts. We assume smoothly varying media for which the wavelength of surface waves is smaller than the scale length of heterogeneity. The monochromatic surface-wave potential  $\chi$  in laterally heterogeneous media can be expressed as,

$$\chi(\mathbf{r}, \omega|\mathbf{r}_s) = \chi_0(\mathbf{r}, \omega|\mathbf{r}_s) + \delta\chi(\mathbf{r}, \omega|\mathbf{r}_s), \quad (3)$$

where  $\chi_0(\mathbf{r}, \omega)$  is a surface-wave potential in a background (reference) model at a frequency  $\omega$ , and  $\delta\chi$  is a perturbed potential of surface waves generated by lateral heterogeneity.

The surface-wave potential  $\chi$  corresponds to a scalar-type wave and is written as  $\chi = A \exp(i\psi)$ , where the amplitude  $A$  and the phase  $\psi$  are slowly varying functions of locations  $\mathbf{r}$ . Although the actual surface wavefields in 3-D media should have a vector form as in (1) and (2), the phase term of the surface waves can be represented by surface-wave potentials. This potential representation allows us a reasonable and efficient treatment of the path effects on the phase of surface waves.

The surface-wave potential  $\chi$  satisfies a spherical Helmholtz equation (Tanimoto 1990; Tromp & Dahlen 1993),

$$[\nabla_1^2 + k^2(\mathbf{r}, \omega)] \chi(\mathbf{r}, \omega | \mathbf{r}_s) = f(\mathbf{r}_s, \omega), \quad (4)$$

where  $\nabla_1^2$  is the surface Laplacian,  $k$  is the wavenumber which is related to surface-wave phase speed  $c(\mathbf{r}, \omega)$  with  $k = \omega/c$ , and  $f$  is a source term at a position  $\mathbf{r}_s$ .

Using the reference phase speed  $c_0(\mathbf{r}, \omega)$ , (4) can be modified to,

$$\left[ \nabla_1^2 + \frac{\omega^2}{c_0^2(\mathbf{r}, \omega)} \frac{c_0^2(\mathbf{r}, \omega)}{c^2(\mathbf{r}, \omega)} \right] \chi(\mathbf{r}, \omega | \mathbf{r}_s) = f(\mathbf{r}_s, \omega), \quad (5)$$

and thus,

$$[\nabla_1^2 + k_0^2(\mathbf{r}, \omega)] \chi(\mathbf{r}, \omega | \mathbf{r}_s) = k_0^2(\mathbf{r}, \omega) \left[ 1 - \frac{c_0^2(\mathbf{r}, \omega)}{c^2(\mathbf{r}, \omega)} \right] \chi(\mathbf{r}, \omega | \mathbf{r}_s) + f(\mathbf{r}_s, \omega), \quad (6)$$

where  $k_0(\mathbf{r}, \omega) = \omega/c_0(\mathbf{r}, \omega)$ . Note that we allow spatial variation of the reference wavenumber  $k_0$  and the reference phase speed  $c_0$ . The term in brackets of right-hand side in (6) can be approximated as,

$$1 - \frac{c_0^2}{c^2} = \frac{c^2 - c_0^2}{c^2} = \frac{2c\delta c - (\delta c)^2}{c^2} \approx \frac{2\delta c}{c}, \quad \text{with } \delta c = c - c_0. \quad (7)$$

Thus (6) can be reduced to,

$$[\nabla_1^2 + k_0^2] \chi(\mathbf{r}, \omega | \mathbf{r}_s) = \frac{2k_0^2\delta c}{c} \chi(\mathbf{r}, \omega | \mathbf{r}_s) + f(\mathbf{r}_s, \omega), \quad (8)$$

where we omit the dependency of phase speed and wavenumber on location  $\mathbf{r}$  and on frequency  $\omega$ . Hereafter, we will omit these variables, unless otherwise specified.

The reference surface-wave potential  $\chi_0$  may also be represented by a scalar Helmholtz equation in the reference medium,

$$[\nabla_1^2 + k_0^2] \chi_0(\mathbf{r}, \omega | \mathbf{r}_s) = f(\mathbf{r}_s, \omega). \quad (9)$$

We now introduce a scalar Green's function  $G(\mathbf{r}, \omega | \mathbf{r}')$  which satisfies,

$$[\nabla_1^2 + k_0^2] G(\mathbf{r}, \omega | \mathbf{r}') = -\delta(\mathbf{r} - \mathbf{r}'), \quad (10)$$

with a boundary condition of outgoing wave radiation as  $\mathbf{r}$  moves away from  $\mathbf{r}'$  (Dahlen 1980). Substituting (3) into (8) and using (9), we obtain

$$[\nabla_1^2 + k_0^2] \delta\chi(\mathbf{r}, \omega | \mathbf{r}_s) = \frac{2k_0^2\delta c}{c} \chi(\mathbf{r}, \omega | \mathbf{r}_s). \quad (11)$$

With the Green's function defined in (10), the perturbed surface-wave potential  $\delta\chi$  may be expressed as,

$$\delta\chi(\mathbf{r}, \omega | \mathbf{r}_s) = \int \int \frac{-2k_0^2\delta c}{c} G(\mathbf{r}, \omega | \mathbf{r}') \chi(\mathbf{r}', \omega | \mathbf{r}_s) d^2\mathbf{r}', \quad (12)$$

where the integration is taken over a sphere. Replacing  $\chi$  in the right-hand side of (12) with a reference surface-wave potential  $\chi_0$  (the first Born approximation),

$$\delta\chi(\mathbf{r}, \omega | \mathbf{r}_s) = \int \int \frac{-2k_0^2\delta c}{c} G(\mathbf{r}, \omega | \mathbf{r}') \chi_0(\mathbf{r}', \omega | \mathbf{r}_s) d^2\mathbf{r}' \quad (13)$$

$$= \int \int K_\chi(\mathbf{r}, \mathbf{r}', \mathbf{r}_s, \omega) \left( \frac{\delta c}{c} \right) d^2\mathbf{r}'. \quad (14)$$

This is a general form of a linearized equation for surface-wave perturbations represented as a spatial integral of the phase-speed perturbation.

If we invert surface waveforms for a model parameter  $\delta m = \delta c/c$  using (14), the general form of the sensitivity kernels  $K_\chi$  for the surface wave potential based on the Born approximation can be represented as,

$$K_\chi(\mathbf{r}, \mathbf{r}', \mathbf{r}_s, \omega) = \left[ \frac{\partial \chi}{\partial m} \right]_\omega = -2k_0^2(\mathbf{r}', \omega) G(\mathbf{r}, \omega | \mathbf{r}') \chi_0(\mathbf{r}', \omega | \mathbf{r}_s). \quad (15)$$

The integral equation (14) shows that the Born kernel  $K_\chi$  relates the phase-speed perturbation to the perturbation of the spectrum of the surface-wave potential, which may be caused by lateral heterogeneity. In most linearized surface-wave tomography for phase-speed structure, we generally work with the phase- and amplitude information separately, and so Rytov's method provides a more direct relation of the phase- and amplitude of surface waves to the model parameters as explained in the next section.

## 2.2 Rytov approach

Now we employ the Rytov approximation for obtaining sensitivity kernels for phase- and amplitude perturbation. In the Rytov method, the logarithm of the wavefield ( $\Phi = \ln \chi$ ) is considered instead of the wavefield itself. We first express the surface-wave potential  $\chi$  as,

$$\chi(\mathbf{r}, \omega | \mathbf{r}_s) = \exp[\Phi(\mathbf{r}, \omega | \mathbf{r}_s)] \quad (16)$$

$$= A(\mathbf{r}, \omega | \mathbf{r}_s) \exp(i\psi(\mathbf{r}, \omega | \mathbf{r}_s)), \quad (17)$$

where  $A$  is the amplitude and  $\psi$  is the phase term for the surface-wave potential. By taking the logarithm,  $\Phi$  can be divided into real and imaginary parts,

$$\Phi = \ln A + i\psi, \quad (18)$$

where we omit the spatial and frequency dependence. Substituting (16) into (8) yields,

$$[\nabla_1^2 + k_0^2] \exp[\Phi] = \frac{2k_0^2 \delta c}{c} \exp[\Phi] + f. \quad (19)$$

Using the relationship  $\nabla_1^2 \exp[\Phi] = \{\nabla_1^2 \Phi + (\nabla_1 \Phi)^2\} \exp[\Phi]$ , (19) can be written as,

$$\nabla_1^2 \Phi + (\nabla_1 \Phi)^2 = -k_0^2 \left(1 - \frac{2\delta c}{c}\right) + f \exp[-\Phi]. \quad (20)$$

Now, let us assume a perturbation of  $\Phi$ ,

$$\Phi = \Phi_0 + \delta\Phi, \quad (21)$$

where  $\Phi_0$  is the logarithm of a reference waveform which will satisfy the equation,

$$\nabla_1^2 \Phi_0 + (\nabla_1 \Phi_0)^2 = -k_0^2 + f \exp[-\Phi_0]. \quad (22)$$

Substituting (21) and (22) into (20) and assuming  $\Phi_0 \gg \delta\Phi$  yields,

$$\nabla_1^2 \delta\Phi + 2\nabla_1 \Phi_0 \nabla_1 \delta\Phi = \frac{2k_0^2 \delta c}{c}, \quad (23)$$

where we neglect a second-order term. By assuming  $\delta\Phi = P(\mathbf{r}, \omega) \exp[-\Phi_0(\mathbf{r}, \omega)]$ , (23) can be reduced to a Helmholtz equation as follows,

$$[\nabla_1^2 + k^2] P(\mathbf{r}, \omega) = \frac{2k_0^2 \delta c}{c} \exp[\Phi_0]. \quad (24)$$

With the Green's function introduced in (10),  $P$  may be expressed as,

$$P(\mathbf{r}, \omega | \mathbf{r}_s) = \delta\Phi e^{\Phi_0} = \int \int \frac{-2k_0^2 \delta c}{c} G(\mathbf{r}, \omega | \mathbf{r}') \exp[\Phi_0(\mathbf{r}', \omega | \mathbf{r}_s)] d^2 \mathbf{r}'. \quad (25)$$

Finally, we obtain an integral equation for  $\delta\Phi$  using  $\chi_0 = \exp[\Phi_0]$ ,

$$\delta\Phi(\mathbf{r}, \omega | \mathbf{r}_s) = \int \int \frac{-2k_0^2 \delta c}{c} \frac{G(\mathbf{r}, \omega | \mathbf{r}') \chi_0(\mathbf{r}', \omega | \mathbf{r}_s)}{\chi_0(\mathbf{r}, \omega | \mathbf{r}_s)} d^2 \mathbf{r}' \quad (26)$$

$$= \int \int K_\Phi(\mathbf{r}, \mathbf{r}', \mathbf{r}_s, \omega) \left(\frac{\delta c}{c}\right) d^2 \mathbf{r}'. \quad (27)$$

Thus the sensitivity kernels for  $\Phi$  can be given by,

$$K_\Phi(\mathbf{r}, \mathbf{r}', \mathbf{r}_s, \omega) = \left[\frac{\partial \Phi}{\partial m}\right]_\omega = -2k_0^2 \frac{G(\mathbf{r}, \omega | \mathbf{r}') \chi_0(\mathbf{r}', \omega | \mathbf{r}_s)}{\chi_0(\mathbf{r}, \omega | \mathbf{r}_s)}. \quad (28)$$

From the relationship (18), the imaginary part of  $K_\Phi$  relates the phase-speed perturbation  $\delta c$  to the phase perturbation  $\delta\psi$  caused by lateral heterogeneity whereas the real part corresponds to the sensitivity for the logarithm of the amplitude term  $A$ . These are explicitly derived from (27),

$$\delta\psi = \int \int \text{Im}\{K_\Phi\} \left(\frac{\delta c}{c}\right) d^2 \mathbf{r}', \quad (29)$$

$$\delta \ln A = \int \int \text{Re}\{K_\Phi\} \left(\frac{\delta c}{c}\right) d^2 \mathbf{r}'. \quad (30)$$

In most surface-wave tomography, the phase perturbation is first measured from observed seismograms, and perturbations are inverted for phase-speed structure. Therefore, the integral eqs (29) and (30) can be used directly for 2-D phase-speed inversion based on the phase- and amplitude measurements for surface waves. In Section 4, we will show examples of the sensitivity kernels mainly focusing on the imaginary part of the Rytov kernels.

### 3 REPRESENTATION OF SENSITIVITY KERNELS WITH ASYMPTOTIC RAY THEORY

#### 3.1 WKBJ approximation

The sensitivity kernels derived in the previous section can be explicitly represented by using the WKBJ approximation (e.g. Tromp & Dahlen 1992; Dahlen & Tromp 1998). Tromp & Dahlen (1993) obtained the scalar Green's function for (10) in a laterally heterogeneous medium

employing the asymptotic results of Dahlen (1980),

$$G(\mathbf{r}, \omega|\mathbf{r}') = \left[ \frac{1}{8\pi k(\mathbf{r})J(\mathbf{r}, \mathbf{r}')} \right]^{\frac{1}{2}} \exp i \left\{ \int_l k d\mathbf{r} + \frac{\pi}{4} \right\}, \quad (31)$$

where  $J$  is a geometrical spreading factor ( $J = \sin \Delta$  for a spherically symmetric earth, where  $\Delta$  is the epicentral distance),  $l$  represents a ray path from  $\mathbf{r}'$  to  $\mathbf{r}$ . Note that we omit a term associated with the Maslov index (Tromp & Dahlen 1992), which represents the number of caustics along a ray path. Here we only consider surface waves passing along minor arcs (i.e. R1 & G1).

Following the WKBJ theory in Tromp & Dahlen (1992), the reference surface-wave potential  $\chi_0$  in (15) and (28) may be represented as,

$$\chi_0(\mathbf{r}, \omega|\mathbf{r}_s) = \left[ \frac{1}{8\pi k(\mathbf{r})J(\mathbf{r}, \mathbf{r}_s)} \right]^{\frac{1}{2}} S(\mathbf{r}, \mathbf{r}_s, \omega) \exp i \left\{ \int_l k d\mathbf{r} + \frac{\pi}{4} \right\}, \quad (32)$$

where  $S(\mathbf{r}, \mathbf{r}_s, \omega)$  is the source term for a moment tensor source radiated toward  $\mathbf{r}$  from the source location  $\mathbf{r}_s$ , which can be given as the contraction of the moment tensor  $\mathbf{M}$  and the conjugate source strain tensor  $\mathbf{E}_s^*$  as follows (Dahlen & Tromp 1998, Section 16.5.2),

$$S(\mathbf{r}, \mathbf{r}_s, \omega) = -\frac{i}{\omega} (\mathbf{M} : \mathbf{E}_s^*), \quad (33)$$

which, for Love waves, takes the form

$$\begin{aligned} \mathbf{M} : \mathbf{E}_s^* &= i(\partial_r W_s - r_s^{-1} W_s) (M_{r\theta} \sin \zeta_s - M_{r\phi} \cos \zeta_s) \\ &- r_s^{-1} k_s W_s \left[ \frac{1}{2} (M_{\theta\theta} - M_{\phi\phi}) \sin 2\zeta_s - M_{\theta\phi} \cos 2\zeta_s \right], \end{aligned} \quad (34)$$

and for Rayleigh waves,

$$\begin{aligned} \mathbf{M} : \mathbf{E}_s^* &= M_{rr} \partial_r U_s + r_s^{-1} \left( U_s - \frac{1}{2} k_s V_s \right) (M_{\theta\theta} + M_{\phi\phi}) \\ &+ i(\partial_r V_s - r_s^{-1} V_s + r_s^{-1} k_s U_s) (M_{r\phi} \sin \zeta_s + M_{r\theta} \cos \zeta_s) \\ &- r_s^{-1} k_s V_s \left[ M_{\theta\phi} \sin 2\zeta_s + \frac{1}{2} (M_{\theta\theta} - M_{\phi\phi}) \cos 2\zeta_s \right]. \end{aligned} \quad (35)$$

Here  $\zeta_s$  is the take-off azimuth at the source measured counter-clockwise from south,  $r_s$  is the radius of the source depth,  $k_s$  is the wavenumber at the source, and  $U_s, V_s$  and  $W_s$  are eigenfunctions at  $r_s$ . The notation used for the moment tensor component ( $M_{rr}, M_{\theta\theta}, M_{\phi\phi}, M_{r\theta}, M_{r\phi}$ , and  $M_{\theta\phi}$ ) is that for the Harvard CMT solutions. We have employed the same normalization convention as used in Tromp & Dahlen (1992). Although we have assumed 2-D scalar wave propagation, the source term  $S$  still requires eigenfunctions at the source location. We may employ a spherical reference model with appropriate crustal corrections for the source location to calculate the eigenfunctions at the source.

Using (31) and (32), the explicit form of the sensitivity kernels (15) and (28) can be derived. For the Born sensitivity kernels,

$$K_\chi(\mathbf{r}, \mathbf{r}', \mathbf{r}_s, \omega) = -\frac{k_0}{4\pi} \left[ \frac{1}{J(\mathbf{r}, \mathbf{r}')J(\mathbf{r}', \mathbf{r}_s)} \right]^{\frac{1}{2}} S(\mathbf{r}, \mathbf{r}_s, \omega) \exp i \left( \int_{l_1} k d\mathbf{r} + \int_{l_2} k d\mathbf{r} + \frac{\pi}{2} \right), \quad (36)$$

where  $l_1$  and  $l_2$  show ray paths from  $\mathbf{r}'$  to  $\mathbf{r}$  and from  $\mathbf{r}_s$  to  $\mathbf{r}'$ , respectively.

Similarly, the explicit expression for the Rytov kernels can be given by,

$$\begin{aligned} K_\Phi(\mathbf{r}, \mathbf{r}', \mathbf{r}_s, \omega) &= -k_0^{\frac{3}{2}} \left[ \frac{1}{2\pi} \right]^{\frac{1}{2}} \left[ \frac{J(\mathbf{r}, \mathbf{r}_s)}{J(\mathbf{r}, \mathbf{r}')J(\mathbf{r}', \mathbf{r}_s)} \right]^{\frac{1}{2}} \frac{S(\mathbf{r}', \mathbf{r}_s, \omega)}{S(\mathbf{r}, \mathbf{r}_s, \omega)} \\ &\times \exp i \left( \int_{l_1} k d\mathbf{r} + \int_{l_2} k d\mathbf{r} - \int_{l_0} k d\mathbf{r} + \frac{\pi}{4} \right), \end{aligned} \quad (37)$$

where  $l_0$  represents a ray path from  $\mathbf{r}_s$  to  $\mathbf{r}$ . For practical calculations for these kernels, we may evaluate the geometrical spreading  $J$  by  $J = \sin X$ , where  $X$  is the distance along a ray path, and the integrations of wavenumbers along ray paths in laterally heterogeneous structures can be done by an iterative use of two-point ray shooting.

### 3.2 Phase term in the sensitivity kernels

The exponential term in (37) can be replaced by,

$$\exp i \left( \psi_1 + \psi_2 - \psi_0 + \frac{\pi}{4} \right), \quad (38)$$

where  $\psi = \int k d\mathbf{r}$ . This phase term may be represented by using the results of the paraxial Fresnel-area ray tracing in the ray centered coordinate system ( $s, n$ ) as described in Yoshizawa & Kennett (2002),

$$\delta\psi_F = \psi_1 + \psi_2 - \psi_0 = \frac{1}{2} n^2 M(s), \quad (39)$$

where  $n$  is a coordinate perpendicular to the ray path,  $s$  is a coordinate along the ray path, and  $M(s) = \frac{\partial^2 \psi(s, n)}{\partial n^2}$  is the second derivatives of phase at ( $s, n$ ) with respect to the perpendicular distance  $n$  from the central ray. (See eq. 16 of Yoshizawa & Kennett 2002, for details).

The phase term in (38) provides an interesting feature of the ray theoretical sensitivity kernels. Just on the central ray, the distance from the central ray  $n$  in (39) is zero, hence  $\delta\psi_F = 0$ . Thus, the exponential term in (37) is always  $\exp i(\pi/4)$  on the central ray path and hence the sensitivity for the surface-wave phase will not be zero on the ray, unlike body wave sensitivity kernels with similar approximation. This fact is also pointed out in Spetzler *et al.* (2002) and Zhou *et al.* (2004).

Note that the paraxial representation of phase term (39) provides us with the possibility of constructing the sensitivity kernels (37) with a simple calculation using hybrid ray tracing as in Yoshizawa & Kennett (2002). However, the paraxial ray approximation can only be used within the range of the first few Fresnel zones since the paraxial ray theory is only valid near the central ray path. Besides, the paraxial ray approximation provides kernels that are always symmetric with respect to the central paths, because it just depends on the velocity gradient along the path (e.g. Yoshizawa 2002). Thus, it is valid only for very limited cases for laterally homogeneous or slowly varying media. In this study, we avoid the use of the paraxial ray approximation for the phase term, but, in the following section, we calculate all the sensitivity kernels with repeated two-point ray calculations for a number of source–scatterer and scatterer–receiver pairs.

#### 4 2-D SENSITIVITY KERNELS FOR SURFACE-WAVE PHASE-SPEED STRUCTURE

In this section, we display examples of sensitivity kernels derived from the Born and Rytov approximation in phase-speed structures.

##### 4.1 Sensitivity kernels in a homogeneous model

We first display the Born and Rytov sensitivity kernels in laterally homogeneous reference model (PREM; Dziewonski & Anderson 1981) for paths from a source near Vanuatu to Australia. Fig. 1 displays the real and imaginary parts of the Born sensitivity kernels for the fundamental-mode Rayleigh wave potential at 0.02 Hz, calculated with the effects of source radiation from a source at 50-km depth shown in Fig. 2. The white area around the great-circle in the imaginary part is equivalent to the first Fresnel zone. Fig. 3 displays the imaginary parts of the Rytov

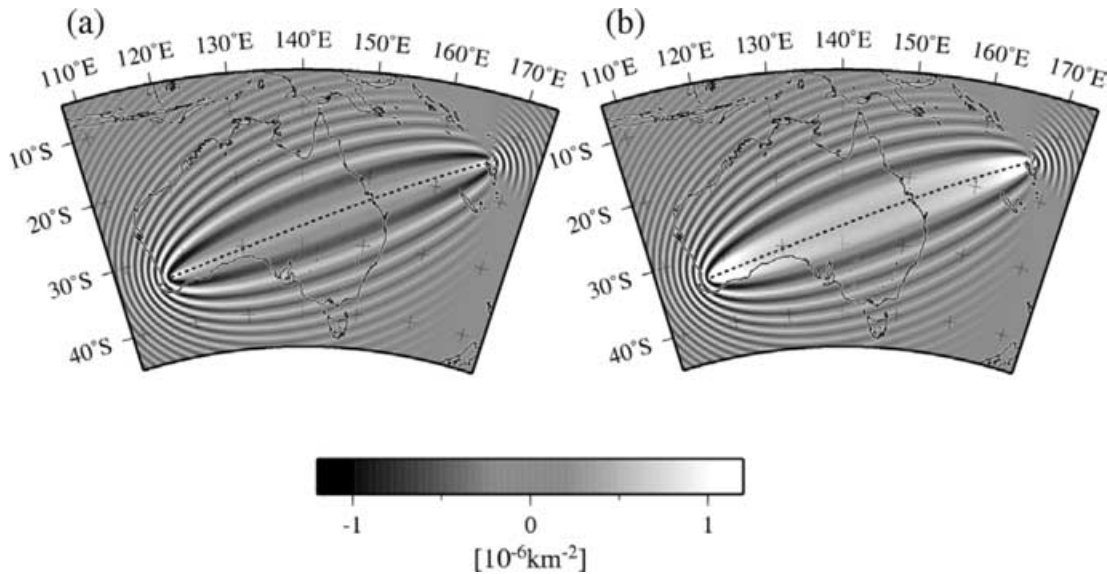


Figure 1. (a) Real- and (b) imaginary parts of the Born sensitivity kernels for a surface-wave potential in a homogeneous reference model including the effects of source radiation of fundamental mode Rayleigh wave at 0.02 Hz for paths from Vanuatu to station NWAO. The dotted line is the great-circle.

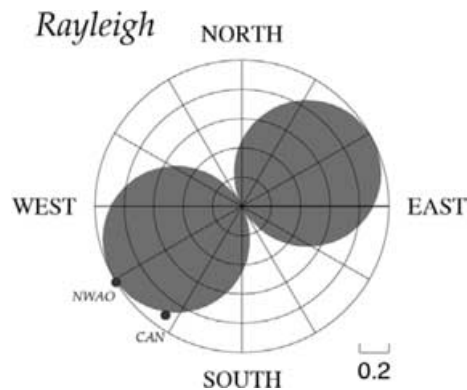
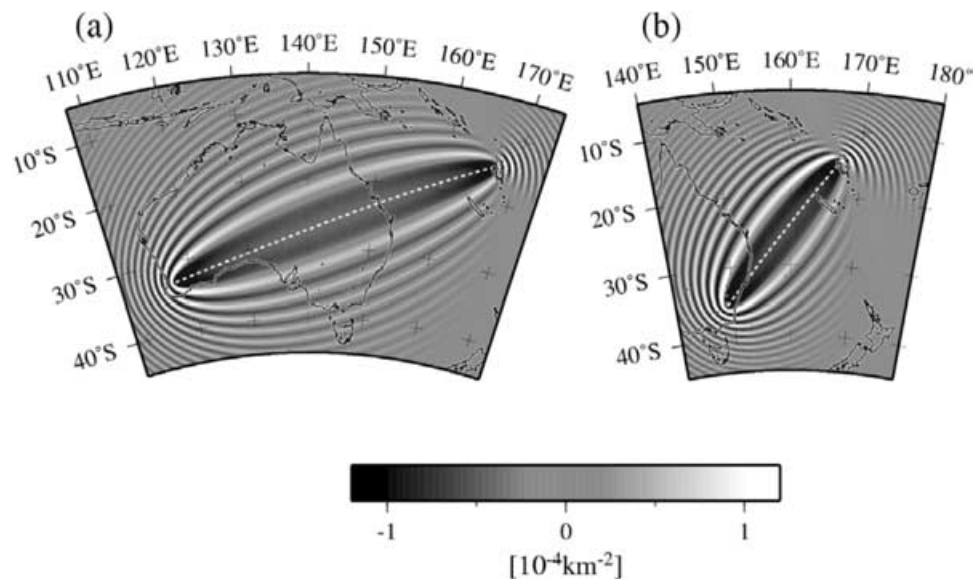


Figure 2. Rayleigh wave radiation pattern for the source parameters used for the calculations of sensitivity kernels. The directions for the two stations, CAN and NWAO, are indicated with dots.





**Figure 3.** Imaginary part of the Rytov sensitivity kernels for fundamental mode Rayleigh wave potential at 0.02 Hz for a homogeneous reference model with the effects of source radiation for paths from Vanuatu to stations (a) NWA0 and (b) CAN. The imaginary part of the Rytov kernels corresponds to the sensitivity kernels for phase perturbations of surface waves. The dotted line is the great-circle.

sensitivity kernels, which corresponds to Fréchet derivatives for the phase variation of Rayleigh wave at periods of 0.02 Hz with the effects of radiation from the source.

Since we only consider sensitivity kernels for monochromatic surface waves at a particular frequency and also ignore the directional dependence of surface-wave scattering in our 2-D treatment, there remain conspicuous side lobes in the outer regions for both the Born and Rytov kernels. Such side lobes of the sensitivity kernels can be reduced when directional scattering in a 3-D structure is considered as discussed in Zhou *et al.* (2004). The side lobes of the kernels are also suppressed when we consider band-limited kernels and only the sensitivities around the lower order Fresnel zones remain (Woodward 1992). This result will be checked through the development of the finite bandwidth kernels in Section 4.3 and the 3-D sensitivity kernels at finite bandwidth in Section 5.

It is worth noting that the longer paths corresponding to the outer oscillations of the sensitivity kernels correspond to time shifts of more than half the period. For a monochromatic wave the  $2\pi$  ambiguity in phase maps them into the same oscillation. But, in a real seismogram composed of a superposition of many frequencies, the influence of the outer lobes will shift to later cycles in the waveform.

In both phase- and amplitude kernels, we see that the maximum sensitivities are not on the centre path nor are they zero there, unlike 3-D sensitivity kernels (banana–doughnut kernels) for body waves based on ray theory (e.g. Yomogida 1992; Dahlen *et al.* 2000; Hung *et al.* 2000). The sensitivity varies along the path and the largest sensitivities are seen near the source- and receiver locations. The longer the periods, the wider is the width of the Fresnel zones and the maximum sensitivity becomes somewhat smaller than the shorter period.

The cross-path profiles of the Rytov kernels in Fig. 3 for the middle of the path as a function of the distance from the central path are displayed in Fig. 4. The sensitivity patterns for a path to CAN exhibit an asymmetric amplitude of the sensitivity due to the effects of source radiation (Fig. 4b). On the other hand, for a path to station NWA0, which is located in the direction of the maximum source radiation, the cross-profiles at the middle of the path (Fig. 4a) do not show any conspicuous effect from the radiation pattern, and are almost symmetric with respect to the central path.

In either case, the oscillation cycle of the kernels as a function of the distance from the central path (Fig. 4) is not affected by the source radiation, suggesting that the elliptical patterns of the Fresnel areas simply depend on the background phase-speed structure and that the source radiation only affects the magnitude and the polarity of the sensitivity.

An opposite polarity of the sensitivity kernels due to the initial phase differences of the source radiation is seen on the northeastern side of the source. The results shown in Figs 3 and 4 also suggest that the sensitivity becomes broader for the longer path (i.e. a path for NWA0). Furthermore, we can see that the longer path tends to have somewhat smaller sensitivity in the middle of the path, compared to the shorter path to station CAN. The fact that a longer path tend to have smaller sensitivity can also be anticipated by ray theory, since the sensitivity per unit length (or area) should be conserved.

## 4.2 Sensitivity kernels in phase-speed models

The Born and Rytov sensitivity kernels in (36) and (37) can be calculated for heterogeneous background media. We further investigate the Rytov sensitivity kernels in a fundamental mode Rayleigh wave phase-speed model in the Australasian region at 0.02 Hz derived by Yoshizawa & Kennett (2004).



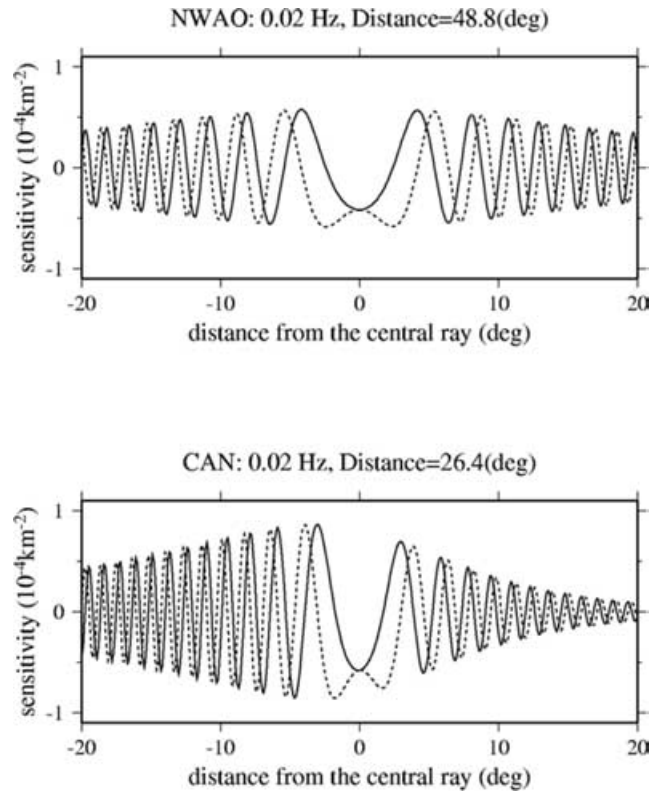


Figure 4. Cross-profiles of the Rytov sensitivity kernels in Fig. 3 at the middle of the path as a function of distance from the central ray. The phase kernel (imaginary part) is shown by a dotted line and amplitude kernels (real part) by a solid line.

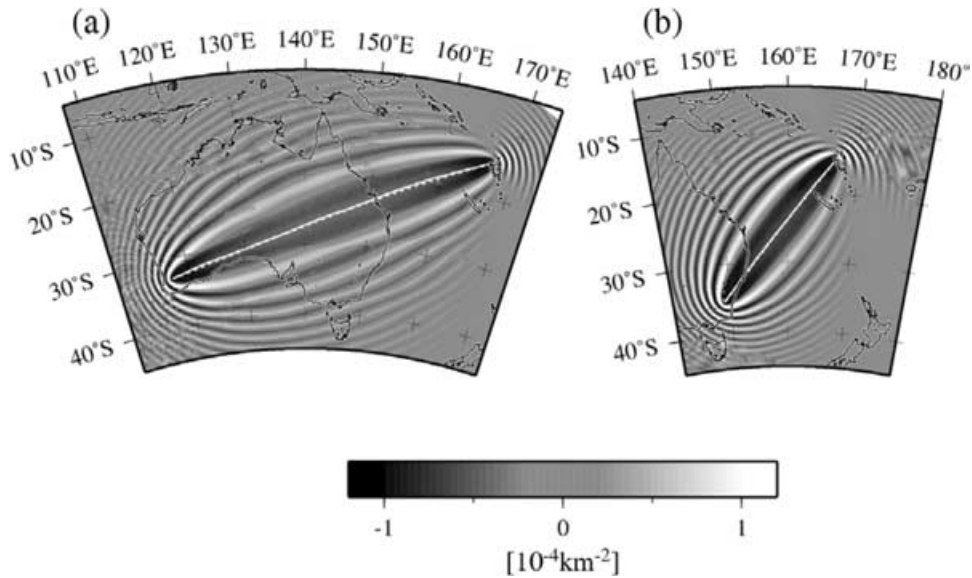
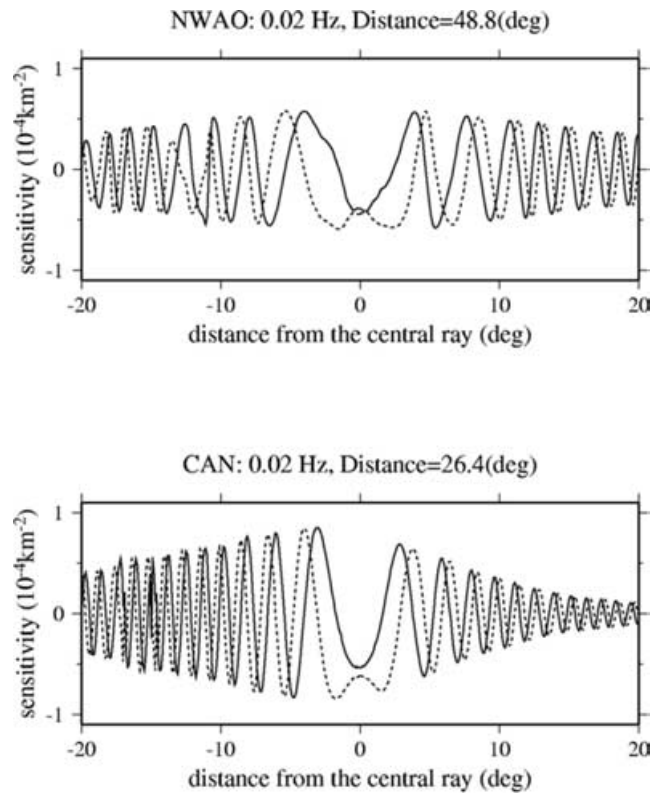


Figure 5. Imaginary part of Rytov sensitivity kernels for fundamental mode Rayleigh wave potential at 0.02 Hz in a Rayleigh wave phase-speed model of Yoshizawa & Kennett (2004) for paths to stations (a) NAWO and (b) CAN. The white dotted line is the great-circle and the solid line the corresponding ray path. All kernels include the effects of source radiation.

For a path to station CAN in Fig. 5(b), the pattern of sensitivity kernels are similar to those for a homogeneous medium in Fig. 3(b). The ray path in this heterogeneous model is not appreciably different from the corresponding great-circle. The similarity of these kernels is also seen in Fig. 6(b), suggesting that there is little effect of the lateral heterogeneity on the sensitivity kernels for this path. This is mainly because that the velocity gradients across the path are smooth around this ray path.

On the other hand, for a path to NAWO in Fig. 5(a), there are some differences from the homogeneous media results shown in Fig. 3(a). The distortion of the sensitivity kernels in the heterogeneous background medium is more apparent in the cross-profile of these kernels in



**Figure 6.** Cross-profiles of the Rytov sensitivity kernels in Fig. 5 at the middle of the path as a function of distance from the central ray. Phase kernel (imaginary part) is shown by a dotted line and amplitude kernels (real part) by a solid line.

Fig. 6(a). The kernels in Figs 5(a) and 6(a) are no longer symmetric with respect to the central path, although the ray path does not show a significant deviation from the corresponding great-circle.

In Fig. 6(a) for station NWAO, the cross-profile of the sensitivity kernel is slightly elongated toward the left-hand side compared to the right-hand side with respect to the central ray path. This implies differences in the distribution of velocity gradient to the northern and southern sides of the paths to NWAO. It should be noted that the asymmetric amplitudes in the kernels in Fig. 6(b) for station CAN are caused by the effects of source radiation, not by the differences in the velocity distribution in the structure.

The differences between Figs 3(a) and 5(a) indicate the importance of the effects of lateral heterogeneity in the background media for which the sensitivity kernels are evaluated. Thus, the use of sensitivity kernels for a laterally heterogeneous background model is needed to make the perturbations of tomographic models small relative to the background model. Although computationally more expensive than the use of sensitivity kernels for a homogeneous background model, a significant enhancement of the resolution of tomography models can be expected.

### 4.3 Sensitivity kernels for finite bandwidth

So far, we have displayed several examples of sensitivity kernels for monochromatic surface waves at a single frequency. However, actual phase-speed data are measured not at a single frequency, but with a certain frequency range with an appropriate bandpass filter. In this section, we discuss the sensitivity kernels by taking a weighted average over certain frequency ranges with narrow band Gaussian filters shown in Fig. 7.

Fig. 8 displays finite bandwidth sensitivity kernels for a homogeneous reference model for the same path as in Fig. 3, and Fig. 9 displays the cross-profiles of Fig. 8. Narrow band Gaussian filters around 0.02 Hz and 0.01 Hz (Fig. 7) are used to construct these finite bandwidth kernels.

The side lobes, which are apparent in Fig. 3, are suppressed in Fig. 8 and just the structural sensitivity near the first few Fresnel zones remains. For the lower frequency range around 0.01 Hz in Figs 8(c) and (d), the width of the Fresnel zones becomes wider, since the horizontal extent of the sensitivity kernels depends on the phase speed at the corresponding frequency in the background structure. It should be noticed that, in this example, the maximum amplitude of the sensitivity kernels at 0.01 Hz is somewhat smaller than that at 0.02 Hz. This is mainly due to the wavenumber-dependent term in (37); that is, the amplification factor by  $k_0^{3/2}$ . The wavenumber  $k_0$  at 0.01 Hz is less than half of that at 0.02 Hz, and thus the  $k_0^{3/2}$  term at 0.01 Hz becomes nearly one-third that at 0.02 Hz.

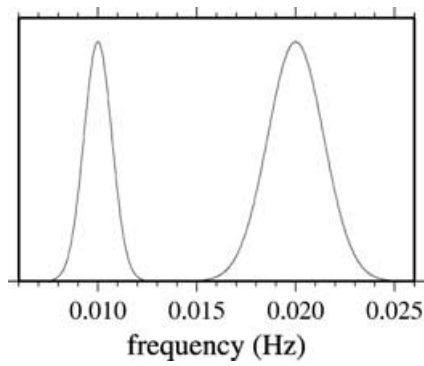


Figure 7. Gaussian band-pass filters centred at 0.01 Hz and 0.02 Hz, which are used to calculate the finite bandwidth kernels in Fig. 8.

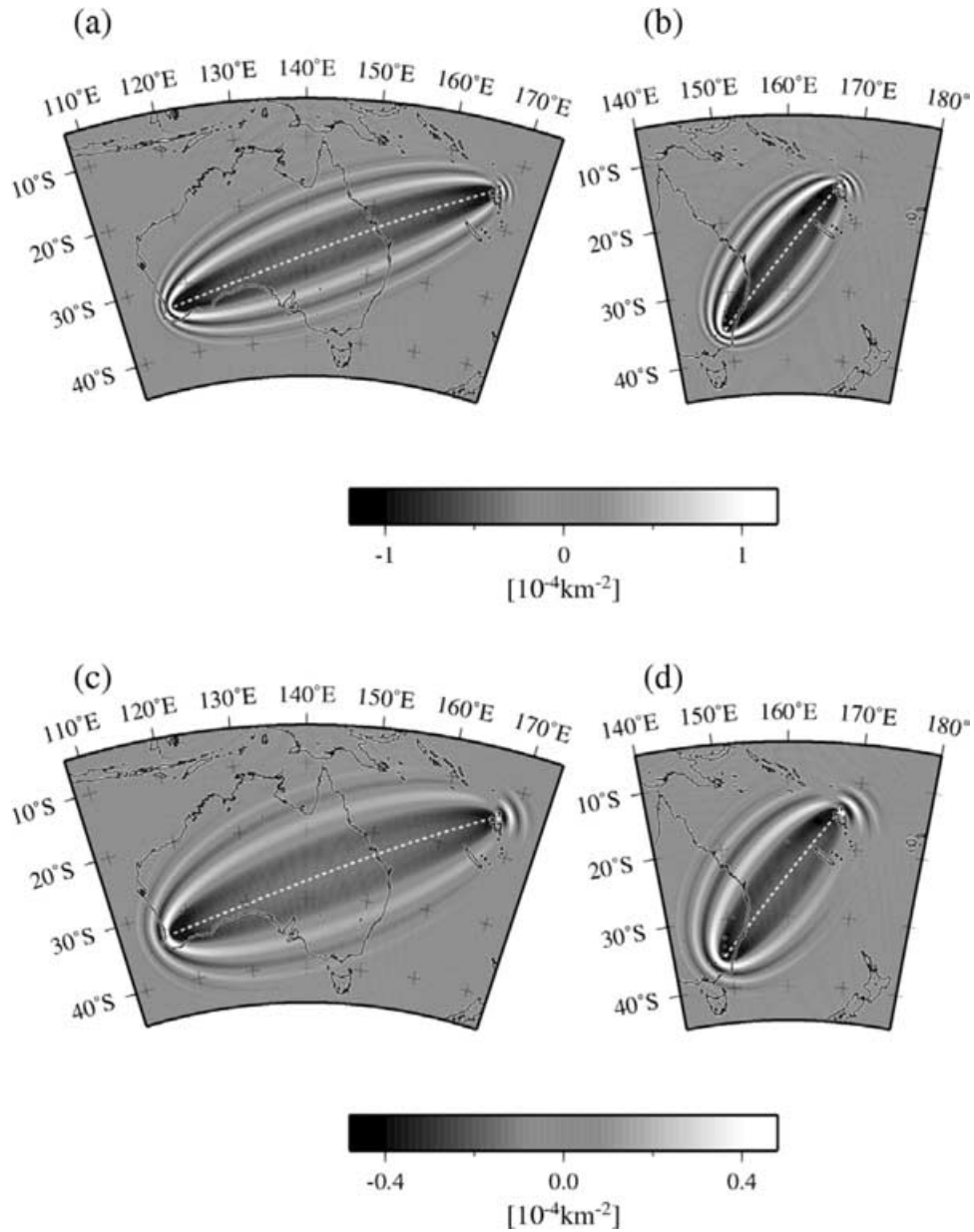
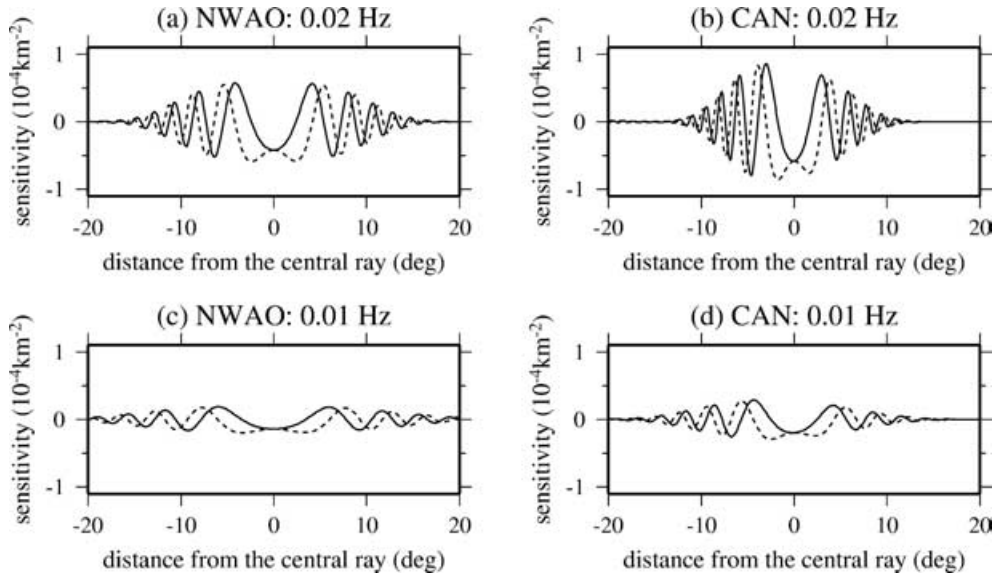


Figure 8. Finite bandwidth sensitivity kernels (imaginary part of the Rytov kernels) of fundamental mode Rayleigh wave potential for a homogeneous reference model, calculated by using narrow band Gaussian filters in Fig. 7 at (a, b) 0.02 Hz and (c, d) 0.01 Hz including the effects of source radiation for paths from Vanuatu to stations (a, c) NAWO and (b, d) CAN. The dotted line is the great-circle.



**Figure 9.** Cross-profiles of the finite bandwidth Rytov sensitivity kernels in Fig. 8 at the middle of the path, as a function of distance from the central ray. The phase kernel (imaginary part) is shown by a dotted line and the amplitude kernels (real part) by a solid line.

## 5 EXTENDED 3-D SENSITIVITY KERNELS

So far, we have mainly focused on the sensitivity kernels for phase-speed structures in the frequency domain. Utilizing these 2-D kernels, in this section, we further extend the kernels to a 3-D case in the time domain, which directly relate the waveform perturbations and shear wave-speed perturbations.

### 5.1 Formulation

As shown in Section 2, using the Born approximation, a perturbation of the surface-wave potential can be expressed in terms of sensitivity kernels for phase-speed structure,

$$\delta\chi(\mathbf{r}, \omega) = \iint K_\chi(\mathbf{r}') \frac{\delta c(\mathbf{r}', \omega)}{c} d^2\mathbf{r}'. \quad (40)$$

Recalling eqs (1) and (2), the perturbation of surface-wave potentials can be related to the displacement field with a vector operator. Utilizing the expression for the Born sensitivity kernel for the surface-wave potential  $K_\chi$ , we can construct waveform sensitivity kernels  $K_u$  for surface waves as discussed in Appendix A. We now consider a sensitivity kernel for a vertical waveform,  $K_u$ . The vertical component of the waveform perturbation,  $\delta u$ , can then be given as,

$$\delta u(\mathbf{r}, \omega) = \iint K_u(\mathbf{r}') \frac{\delta c(\mathbf{r}', \omega)}{c} d^2\mathbf{r}', \quad (41)$$

where  $K_u$  is given explicitly in Appendix A.

Local phase-speed perturbations can be expressed in terms of 1-D sensitivity kernels for a reference Earth model and local shear wave-speed perturbations  $\delta\beta$ ,

$$\frac{\delta c(\mathbf{r}, \omega)}{c} = \int_0^a K_\beta(r, \omega) \frac{\delta\beta(\mathbf{r}, r)}{\beta} dr, \quad (42)$$

where  $K_\beta(r, \omega) = (\beta/c) [\partial c / \partial \beta]$  is a local 1-D sensitivity kernel to shear wave speed (Takeuchi & Saito 1972; Dahlen & Tromp 1998), and the integration is taken over the Earth's radius  $a$ . Some examples of 1-D sensitivity kernels  $K_\beta$  are given in Fig. 10 together with the sensitivity kernels to  $P$ -wave speed ( $K_\alpha$ ) and density ( $K_\rho$ ). Since the contribution of  $P$ -wave speed and density to surface-wave-phase speed is not as significant as that of shear wave speed, we consider just the shear wave-speed perturbation in (42).

Substituting (42) into (41), we can derive a linearized relationship between waveform perturbation and a local shear wave-speed perturbation as follows,

$$\delta u(\mathbf{r}, \omega) = \iint d^2\mathbf{r}' \int dr K_u(\mathbf{r}', \omega) K_\beta(r, \omega) \frac{\delta\beta(\mathbf{r}', r)}{\beta}. \quad (43)$$

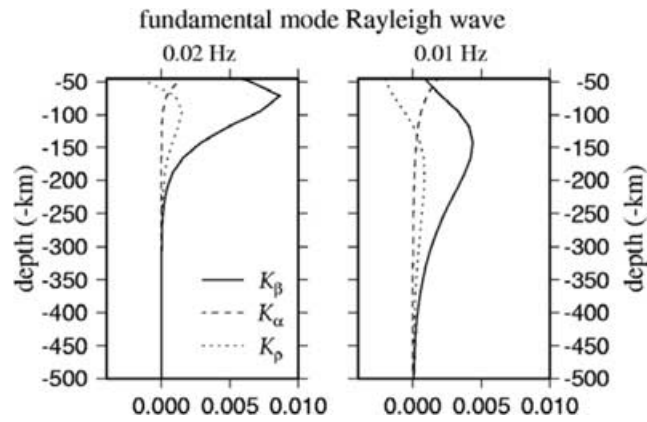


**Figure 10.** 1-D sensitivity kernels of fundamental mode Rayleigh waves at (left) 0.02 Hz and (right) 0.01 Hz for  $P$ - and  $S$ -wave speed, and density perturbations.

Taking the inverse Fourier transform of the above yields 3-D sensitivity kernels in the time domain as follows,

$$\begin{aligned}
 \delta u(\mathbf{r}, t) &= \frac{1}{2\pi} \int \delta u(\mathbf{r}, \omega) \exp\{i\omega t\} d\omega \\
 &= \frac{1}{2\pi} \int \int d^2\mathbf{r}' \int dr \int d\omega K_u(\mathbf{r}', \omega) K_\beta(r, \omega) \exp\{i\omega t\} \frac{\delta\beta(\mathbf{r}', r)}{\beta} \\
 &= \int \int d^2\mathbf{r}' \int dr K^{3D}(\mathbf{r}', r, t) \frac{\delta\beta(\mathbf{r}', r)}{\beta},
 \end{aligned} \tag{44}$$

where the 3-D kernel can be expressed as,

$$K^{3D}(\mathbf{r}', r, t) = \frac{1}{2\pi} \int d\omega K_u(\mathbf{r}', \omega) K_\beta(r, \omega) \exp\{i\omega t\}. \tag{45}$$

This expression for the 3-D kernel provides us with a direct linearized relationship between shear wave-speed perturbation  $\delta\beta$  and waveform perturbation  $\delta u$  in the time domain for a particular frequency range. Such 3-D kernels allows us to invert the perturbations in observed waveform into 3-D shear wave-speed structure taking account of the effects of finite frequency, without the intermediary process of phase-speed measurements.

## 5.2 Examples of 3-D sensitivity kernels in the time domain

Here we show examples of 3-D waveform sensitivity kernels for the vertical component of the fundamental-mode Rayleigh waves. For simplicity in numerical computation, we focus on the behaviour of the kernels in a laterally homogeneous background structure. The path is the same as in Fig. 1.

Fig. 11 displays a synthetic seismogram for a reference model at an epicentral distance of 48.8 degrees as well as the evolution of the waveform sensitivity kernels as a function of time. The frequency range used to calculate the kernel is from 0.010 to 0.033 Hz. PREM is used as the reference model and the source depth is at 50 km. Horizontal slices at 94-km depth and vertical cross-path sections at the middle of the paths are displayed in Fig. 11. At the initial portion of the fundamental-mode Rayleigh wave at an elapsed time of 1400 s (Fig. 11a), sensitivity is concentrated around the centre path. With the passage of Rayleigh waves across the station, as marked on the synthetic seismogram, the regions of sensitivity gradually spread out from the path toward the outer regions, retaining strong sensitivity near the source and receiver regions (Figs 11b and c). For the later portion of the Rayleigh wave train the sensitivity to structure near the central ray path is weakened, thereby enhancing sensitivity to structure in regions well away from the ray path. The higher frequency components with greater sensitivity to shallow depths are concentrated near the central paths. In contrast, the lower frequency waves, with higher phase speed, are primarily sensitive to structure in the outer regions. This effect gives rise to the distinctive shape of the lower boundary of the region of maximum sensitivity to structure in Fig. 11(d).

Fig. 12 shows instantaneous sensitivity kernels at 1420 s with different frequency ranges and filtered synthetic seismograms. The lower the frequency range, the wider is the area of sensitivity, that corresponds to the low-order Fresnel zones. This is mainly because phase speeds for lower frequency waves in the background structure are faster than those for higher frequency waves, as we have already seen for the band-limited sensitivity kernels in Section 4.3. The results for the vertical slice at the middle of the path indicate that the Rayleigh waves at lower frequency have more sensitivity to deeper structure, while those at higher frequency dominate the sensitivity to the shallower depth. The maximum amplitude of the sensitivity kernel for higher frequency range (0.02–0.03 Hz) in Fig. 12(c) is more than 60 times larger than that for the lower frequency range shown in Fig. 12(a). (The amplitude of the corresponding waveforms in Fig. 12 are normalized so that each waveform has the equal maximum amplitude.) Lower frequency waves (e.g. lower than 0.01 Hz) are rather weakly radiated from a source at 50-km depth, compared to the higher frequency waves (e.g. higher than 0.02 Hz), which have noticeable sensitivity to the shallower part of the mantle.



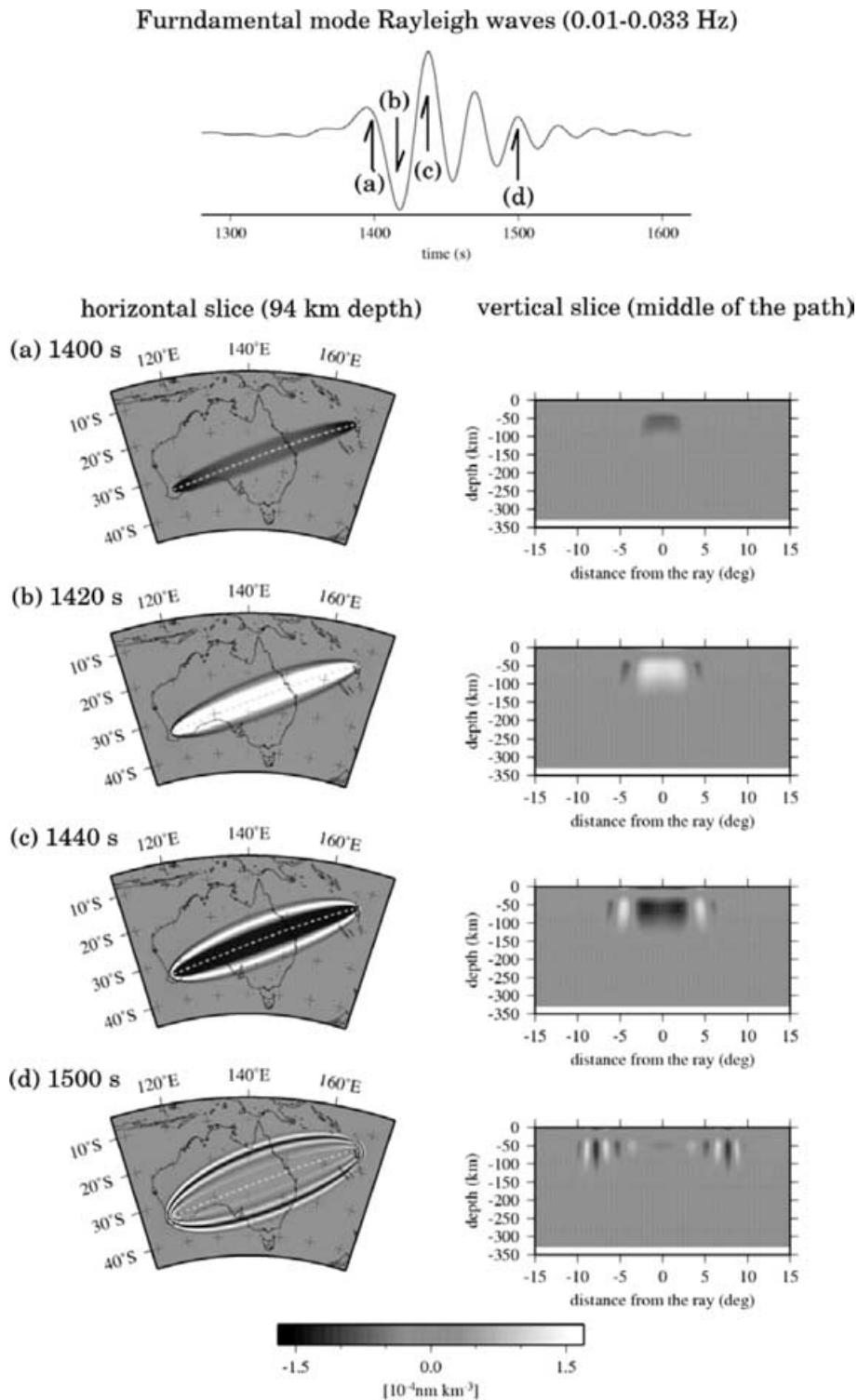


**Figure 11.** A synthetic waveform for the vertical component of fundamental mode Rayleigh waves in a homogeneous medium, and snapshots of 3-D sensitivity kernels as a function of time. Sections through the 3-D sensitivity kernels are shown for a set of horizontal slices at 94-km depth (left column) and vertical cross-sections at the middle of path (right column) for times (a) 1400 s (b) 1420 s, (c) 1440 s, and (d) 1500 s. The frequency range is 0.010–0.033 Hz.

## 6 DISCUSSION

We have derived 2-D sensitivity kernels for surface wave phases and 3-D sensitivity kernels for surface waveforms, based on single scattering theory with the Born and Rytov approximations using a surface-wave-potential representation. The sensitivity kernels shown in this paper will



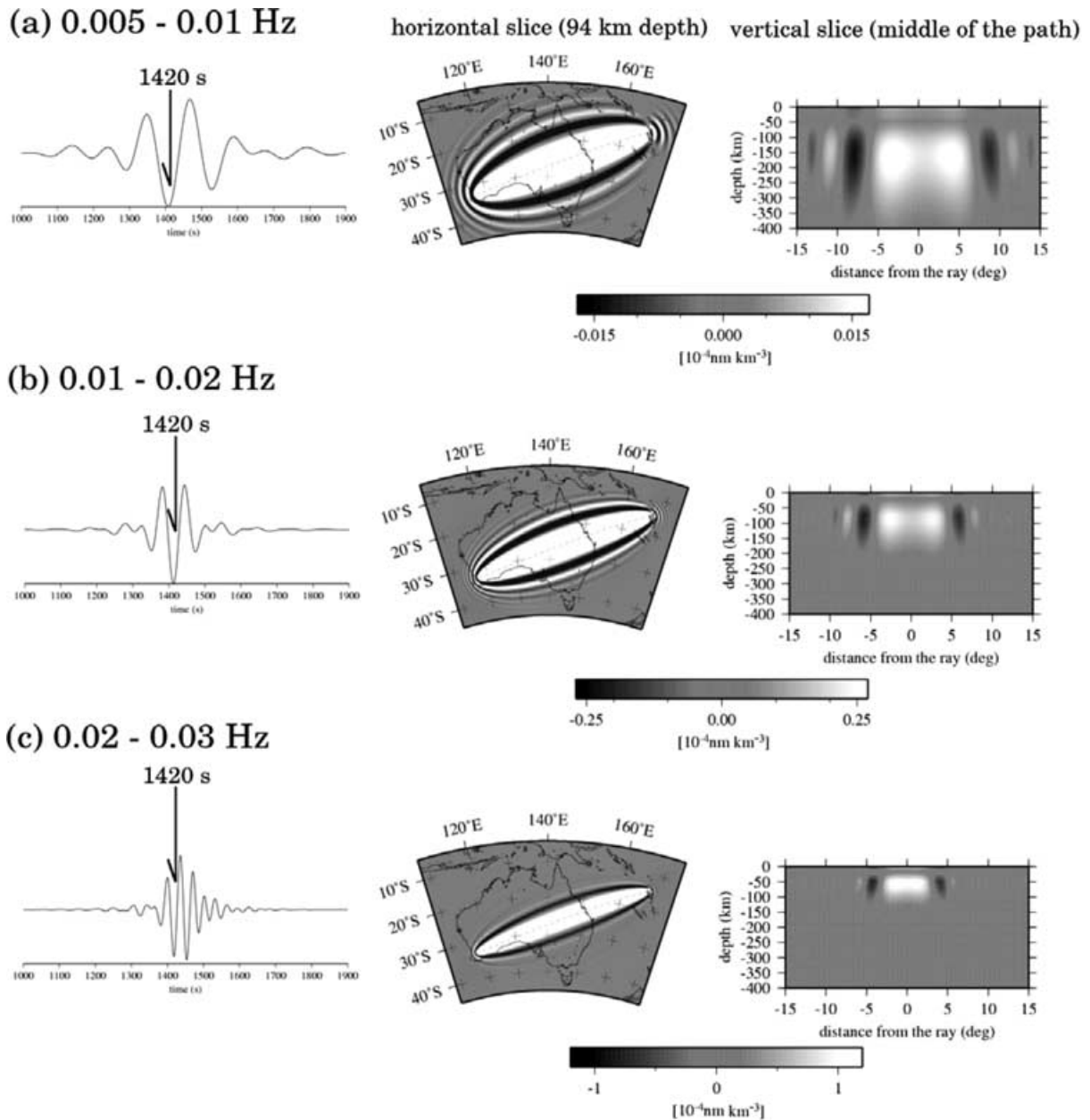


**Figure 12.** Instantaneous 3-D waveform sensitivity kernels at 1420 s with various frequency ranges; (a) 0.005–0.01 Hz, (b) 0.01–0.02 Hz and (c) 0.02–0.03 Hz. The amplitude of the displayed waveforms are normalized so that they share the common maximum amplitude. Note that the maximum amplitude of the sensitivity kernels differs between the frequency ranges mainly because of the differences in the radiated energy at the source.

be helpful to take account of the effects of scattered and diffracted waves from a wide region around the path, which cannot be fully treated with an approximate description of the influence zone (Yoshizawa & Kennett 2002).

For monochromatic waves at a particular frequency, the first-order sensitivity kernels extend over a wide region with very little decrease in the magnitude of the sensitivity away from the central ray path. However, the outside portion of the sensitivity is suppressed in finite bandwidth kernels constructed by superposition of monochromatic sensitivity kernels modulated by a narrow band Gaussian filter response. Also, in the 3-D kernels, the outer parts of the sensitivity zone only affect the later portion of the surface waves. The main portion of the surface waves is sensitive just to the wave-speed structure around the low-order Fresnel zones near the nominal ray path. The later portion of the seismograms can overlap with the scattered signals, and such scattered phases may not be distinguishable in an observed waveform as the surface waves are dispersed. Thus, the use of finite-frequency kernels is important for inversions for a velocity structure when using higher frequency surface waves, which are likely to be affected by scattered phases in the crust and the uppermost mantle.

The Rytov kernels for station NWAO in the laterally heterogeneous structure imply that the effects of strong lateral velocity gradients can significantly affect the shape of the sensitivity kernels. Thus, care must be taken when we use such kernels for higher frequency surface waves.

It should be noted that both the Born and Rytov kernels obtained in this study are based on the use of surface-wave potentials, which corresponds to a scalar wave representation, and the WKBJ approximation. Both the WKBJ and potential theories have similar limitations in the requirement for the background medium to be slowly varying. Thus, mode-branch coupling or the directional dependency of the scattered waves are not fully treated here. The linearized scattering theory of Snieder (1986) and Snieder & Nolet (1987), employed by Zhou *et al.* (2004), can be used to construct surface-wave sensitivity kernels that take account of the coupling between low-order mode branches. However, for a full treatment of these effects, we may need to work with 3-D shear wave-speed models as in Marquering *et al.* (1998, 1999) rather than with phase-speed models, although it would then be more complicated to incorporate the effects of off-great-circle propagation (*cf.* Kennett 1998).

The 2-D and 3-D sensitivity kernels obtained in this study can be calculated fairly efficiently in homogeneous media, although the kernels for laterally heterogeneous models require somewhat heavier computation. The 3-D sensitivity kernels relate the perturbation of observed waveforms directly to shear wave-speed perturbation in three dimension. Thus, it is feasible to perform direct inversion of observed waveforms with suitable multiple bandpass filterers for a 3-D shear wave structure, taking account of the effects of finite frequency.

## ACKNOWLEDGMENTS

We would like to thank Gabi Laske, Barbara Romanowicz and Ying Zhou for their constructive comments, which helped to improve the manuscript. This study was partly supported by a Grant-in-Aid for Scientific Research (No. 15740266) to KY from the Ministry of Education, Culture, Sports, Science and Technology of Japan.

## REFERENCES

- Born, M. & Wolf, E., 1999. *Principles of Optics*, 7th edn, Cambridge Univ. Press, Cambridge.
- Červený, V. & Soares, J.E.P., 1992. Fresnel volume ray tracing, *Geophysics*, **57**, 902–915.
- Dahlen, F.A., 1980. A uniformly valid asymptotic representation of normal mode multiplet spectra on a laterally heterogeneous Earth, *Geophys. J. R. astr. Soc.*, **62**, 225–247.
- Dahlen, F.A., Hung, S.-H. & Nolet, G., 2000. Fréchet kernels for finite-frequency travel times - I. Theory, *Geophys. J. Int.*, **141**, 157–174.
- Dahlen, F.A. & Tromp, J., 1998. *Theoretical Global Seismology*, Princeton Univ. Press, Princeton, New Jersey.
- Devaney, A.J., 1984. Geophysical Diffraction Tomography, *IEEE Trans. Geosci. Remote Sensing*, **GE-22**, 3–13.
- Dziewonski, A.M. & Anderson, D.L., 1981. Preliminary reference Earth model, *Phys. Earth planet. Inter.*, **25**, 297–356.
- Friderich, W., 1999. Propagation of seismic shear and surface waves in a laterally heterogeneous mantle by multiple forward scattering, *Geophys. J. Int.*, **136**, 180–204.
- Gung, Y. & Romanowicz, B., 2004. Q tomography of the upper mantle using three-component long-period waveforms, *Geophys. J. Int.*, **157**, 813–830.
- Hung, S.-H., Dahlen, F.A. & Nolet, G., 2000. Fréchet kernels for finite-frequency travel times—II. Examples, *Geophys. J. Int.*, **141**, 175–203.
- Kennett, B.L.N., 1998. Guided waves in three-dimensional structures, *Geophys. J. Int.*, **133**, 159–174.
- Laske, G., Masters, G. & Zürn, W., 1994. Frequency dependent polarization measurements of long-period surface waves and their implications for global phase velocity maps, *Phys. Earth Planet. Inter.*, **84**, 111–137.
- Li, X.-D. & Tanimoto, T., 1993. Waveforms of long-period body waves in a slightly aspherical Earth model, *Geophys. J. Int.*, **112**, 92–102.
- Li, X.-D. & Romanowicz, B., 1995. Comparison of global waveform inversions with and without considering cross-branch modal coupling, *Geophys. J. Int.*, **121**, 695–709.
- Li, X.-D. & Romanowicz, B., 1996. Global mantle shear velocity model developed using nonlinear asymptotic coupling theory, *J. geophys. Res.*, **101**, 22 245–22 272.
- Luo, Y. & Shuster, G.T., 1991. Wave-equation traveltimes inversion, *Geophysics*, **56**, 645–653.
- Marquering, H. & Snieder, R., 1995. Surface-wave mode coupling for efficient forward modelling and inversion of body-wave phases, *Geophys. J. Int.*, **120**, 186–208.
- Marquering, H., Nolet, G. & Dahlen, F.A., 1998. Three-dimensional waveform sensitivity kernels, *Geophys. J. Int.*, **132**, 521–534.
- Marquering, H., Dahlen, F.A. & Nolet, G., 1999. Three-dimensional sensitivity kernels for finite-frequency travel times: the banana-doughnut paradox, *Geophys. J. Int.*, **137**, 805–815.
- Maupin, V., 2001. A multiple-scattering scheme for modelling surface wave propagation in isotropic and anisotropic three-dimensional structures, *Geophys. J. Int.*, **146**, 332–348.
- Meier, T., Lebedev, S., Nolet, G. & Dahlen, F.A., 1997. Diffraction tomography using multimode surface waves, *J. geophys. Res.*, **102**, 8255–8267.
- Montelli, R., Nolet, G., Dahlen, F.A., Masters, G., Engdahl, E.R. & Hung, S.-H., 2004. Finite-frequency tomography reveals a variety of plumes in the mantle, *Science*, **303**, 338–343.
- Snieder, R., 1986. 3-D linearized scattering of surface waves and a formalism for surface wave holography, *Geophys. J. R. astr. Soc.*, **84**, 581–605.
- Snieder, R. & Lomax, A., 1996. Wavefield smoothing and the effect of rough velocity perturbations on arrival times and amplitudes, *Geophys. J. Int.*, **125**, 796–812.
- Snieder, R. & Nolet, G., 1987. Linearized scattering of surface waves on a spherical Earth, *J. Geophys.*, **61**, 55–63.
- Spetzler, J., Trampert, J. & Snieder, R., 2002. The effects of scattering in surface wave tomography, *Geophys. J. Int.*, **149**, 755–767.
- Takeuchi, H. & Saito, M., 1972. Seismic surface waves, in *Seismology: Surface Waves and Free Oscillations, Methods in Computational Physics*, Vol. 11, pp. 217–295, ed. Bolt, B.A., Academic Press, New York.
- Tanimoto, T., 1990. Modelling curved surface wave paths: membrane surface wave synthetics, *Geophys. J. Int.*, **102**, 89–100.
- Tromp, J. & Dahlen, F.A., 1992. Variational principles for surface wave propagation on a laterally heterogeneous Earth—II. Frequency-domain JWKB theory, *Geophys. J. Int.*, **109**, 599–619.
- Tromp, J. & Dahlen, F.A., 1993. Variational principles for surface wave propagation on a laterally heterogeneous Earth—III. Potential representation, *Geophys. J. Int.*, **112**, 195–209.
- Vasco, D.W. & Majer, E.L., 1993. Wavepath traveltimes tomography, *Geophys. J. Int.*, **115**, 1055–1069.
- Wielandt, E., 1987. On the validity of the ray approximation for interpreting delay times, in *Seismic Tomography*, pp. 85–98, ed. Nolet, G., D. Reidel Publishing Co., Dordrecht.
- Woodward, M.J., 1992. Wave-equation tomography, *Geophysics*, **57**, 15–26.
- Yomogida, K., 1985. Gaussian beams for surface waves in laterally slowly-varying media *Geophys. J. R. astr. Soc.*, **82**, 511–533.
- Yomogida, K., 1992. Fresnel zone inversion for lateral heterogeneities in the Earth, *Pure appl. Geophys.*, **138**, 391–406.
- Yomogida, K. & Aki, K., 1985. Waveform synthesis of surface waves in a laterally heterogeneous earth by the Gaussian beam method, *J. geophys. Res.*, **90**, 7665–7688.

- Yomogida, K. & Aki, K., 1987. Amplitude and phase data inversion for phase velocity anomalies in the Pacific Ocean basin, *Geophys. J. R. astr. Soc.*, **88**, 161–204.
- Yoshizawa, K., 2002. Development and application of new techniques for surface wave tomography, *PhD thesis*, Australian National University, Canberra, p. 204.
- Yoshizawa, K. & Kennett, B.L.N., 2002. Determination of the influence zone for surface wave paths, *Geophys. J. Int.*, **149**, 440–453.
- Yoshizawa, K. & Kennett, B.L.N., 2004. Multimode surface wave to-

mography for the Australian region using a three-stage approach incorporating finite frequency effects, *J. geophys. Res.*, **109**, B02310, doi:10.1029/2002JB002254.

- Zhao, L., Jordan, T.H. & Chapman, C.H., 2000. Three-dimensional Fréchet differential kernels for seismic delay times, *Geophys. J. Int.*, **141**, 558–576.
- Zhou, Y., Dahlen, F.A. & Nolet, G., 2004. Three-dimensional sensitivity kernels for surface wave observables, *Geophys. J. Int.*, **158**, 142–168.

## APPENDIX A: WAVEFORM SENSITIVITY KERNELS

The 2-D waveform sensitivity kernels for surface waves in Section 5 can be represented by using the expressions of the Born sensitivity kernels for surface-wave potentials  $K_\chi$  explained in Sections 2 and 3. With the vector operator in eqs (1) and (2), the total perturbed wavefield  $\delta\mathbf{u}$  can be given by working with perturbed surface-wave potentials for both Rayleigh and Love waves as

$$\delta\mathbf{u}(\mathbf{r}, \omega) = [\mathbf{r}U(r, \omega) + k_R^{-1}V(r, \omega)\nabla_1] \delta\chi_R(\mathbf{r}, \omega) - k_L^{-1}W(r, \omega)\mathbf{r} \times \nabla_1 \delta\chi_L(\mathbf{r}, \omega). \quad (\text{A1})$$

Hereafter we omit the variable dependency on the frequency  $\omega$ .

Using the linearized equation for potential perturbation (40), (A1) can be represented as,

$$\begin{aligned} \delta\mathbf{u}(\mathbf{r}) = & \int \int [\mathbf{r}U(r) + k_R^{-1}V(r)\nabla_1] K_\chi^R(\mathbf{r}') \left( \frac{\delta c(\mathbf{r}')}{c} \right)_R d^2\mathbf{r}' \\ & - \int \int k_L^{-1}W(r)\mathbf{r} \times \nabla_1 K_\chi^L(\mathbf{r}') \left( \frac{\delta c(\mathbf{r}')}{c} \right)_L d^2\mathbf{r}', \end{aligned} \quad (\text{A2})$$

where superscripts and subscripts  $R$  stand for Rayleigh waves and  $L$  for Love waves. Replacing the horizontal gradient terms at the receiver location by working with the wavenumber vector of a scattered wave  $\mathbf{k}' = \nabla_1 \psi'$  ( $\psi'$  is a phase for a scattered wave) that is scattered at a location  $\mathbf{r}'$  and arrives at the receiver (Fig. A1), (A2) can be expressed as,

$$\begin{aligned} \delta\mathbf{u}(\mathbf{r}) = & \int \int [\mathbf{r}U(r) + i\hat{\mathbf{k}}'V(r)] K_\chi^R(\mathbf{r}') \left( \frac{\delta c(\mathbf{r}')}{c} \right)_R d^2\mathbf{r}' \\ & - \int \int i\mathbf{r} \times \hat{\mathbf{k}}'W(r) K_\chi^L(\mathbf{r}') \left( \frac{\delta c(\mathbf{r}')}{c} \right)_L d^2\mathbf{r}', \end{aligned} \quad (\text{A3})$$

where  $\hat{\mathbf{k}}' (= \mathbf{k}'/k)$  is a unit wavenumber vector representing the direction of propagation of a scattered wave at the receiver. Note that we have dropped the subscripts  $R$  and  $L$  for the wavenumber vectors.

Considering the direction of scattered waves at the receiver as shown in Fig. A1, each component of the waveform perturbation  $\delta\mathbf{u} = (\delta u, \delta v, \delta w)$  for vertical, radial and transverse component (defined as in Fig. A1) can be represented as follows,

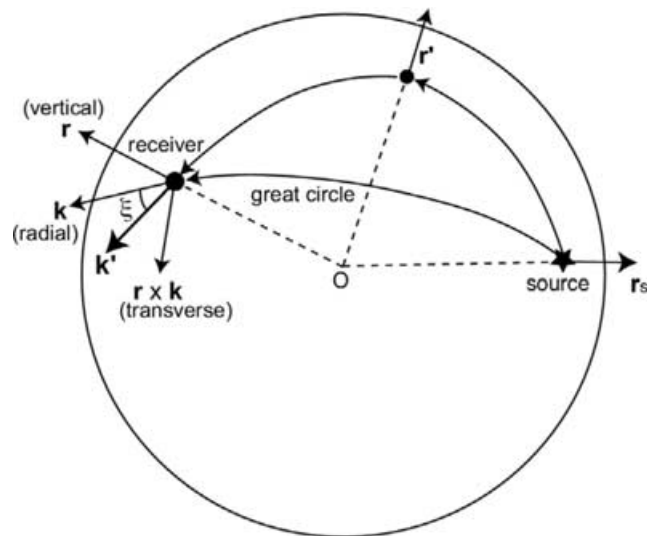


**Figure A1.** Schematic illustration of a source-receiver pair, a scattered wave travelling through the receiver location and the definition of the three components at the receiver. The direction of the wavenumber vector of a scattered wave  $\mathbf{k}'$  is measured counter-clockwise from the great-circle.

$$\delta u = \int \int U(r) K_{\chi}^R \left( \frac{\delta c}{c} \right)_R d^2 \mathbf{r}', \quad (\text{A4})$$

$$\delta v = \int \int \left\{ i V(r) \cos \xi K_{\chi}^R \left( \frac{\delta c}{c} \right)_R + i W(r) \sin \xi K_{\chi}^L \left( \frac{\delta c}{c} \right)_L \right\} d^2 \mathbf{r}', \quad (\text{A5})$$

$$\delta w = \int \int \left\{ -i W(r) \cos \xi K_{\chi}^L \left( \frac{\delta c}{c} \right)_L + i V(r) \sin \xi K_{\chi}^R \left( \frac{\delta c}{c} \right)_R \right\} d^2 \mathbf{r}', \quad (\text{A6})$$

where  $\xi$  is the angle of the wavenumber vector  $\mathbf{k}'$  measured counter-clockwise from the great-circle direction as in Fig. A1. The directional dependence of the horizontal component is similar to the receiver term derived by Zhou *et al.* (2004). The 2-D waveform sensitivity kernels for each component  $K_u = (K_u, K_v, K_w)$  can thus be summarized as,

$$K_u^R = U(r) K_{\chi}^R, \quad (\text{A7})$$

$$K_v^R = i V(r) \cos \xi K_{\chi}^R, \quad K_v^L = i W(r) \sin \xi K_{\chi}^L, \quad (\text{A8})$$

$$K_w^R = i V(r) \sin \xi K_{\chi}^R, \quad K_w^L = -i W(r) \cos \xi K_{\chi}^L. \quad (\text{A9})$$

Working with the local 1-D sensitivity kernels (42), the waveform sensitivity kernel can be used to obtain the 3-D sensitivity kernels as explained in the Section 5.1.